On the understanding of the optoelectronic properties of S-doped MoO 3 and O-doped MoS 2 bulk systems: a DFT perspective

Masoud Shahrokhi, Pascal Raybaud, Tangui Le Bahers

On the understanding of the optoelectronic properties of S-doped MoO_3 and O-doped MoS_2 bulk systems: A DFT Perspective

Masoud Shahrokhi [1], Pascal Raybaud [1,2*] and Tangui Le Bahers [1*]

[1] *Univ Lyon, ENS de Lyon, CNRS, Université Claude Bernard Lyon 1, Laboratoire de Chimie UMR 5182, F-69342 Lyon, France*

[2] *IFP Energies nouvelles, Rond-point de l'échangeur de Solaize, BP 3, 69360 Solaize, France*

Authors for correspondence: pascal.raybaud@ifpen.fr; tangui.le_bahers@ens-lyon.fr

Abstract

First-principles calculations were carried out to understand the structure and optoelectronic properties of α-MoO_3 and 2H-MoS_2 bulk systems with anionic isovalent-atom substitutions. The DFT calculations have been performed by adopting HSE06 functional to probe the optoelectronic structures and Boltzmann transport theory to compute the DOS-averaged effective mass and mobility of studied compounds. Our first principle calculations indicate that substituting oxygen atoms by sulfur atoms on α-MoO_3, the electronic energy gap is decreased from 3.0 eV in pristine material to around 1.6 eV in sulfur doped material. On the other hand, substituting sulfur atoms by oxygen atoms on 2H-MoS_2 does not produce significant change in the electronic band gap. We found that α-MoO_3 with high sulfur concentrations ($x_s \geq 33\%$) is thermodynamically stable and possess ideal dielectric function, optical, charge transport and exciton binding energy for photocatalytic applications while for lower concentrations the carriers mobility is restricted due to the high value of carriers effective masses induced by localized electronic states. Probing the photocatalytic parameters for oxygen substituted 2H-MoS_2 bulk system shows that this sulfide is not deeply altered by oxygen incorporation.

1. Introduction

In the quest for alternative approaches of producing clean fuels and chemicals, photocatalysis may represent an alternative and appealing pathway. However, one challenging bottleneck among others remains the improvement of the opto-electronic properties of the semi-conducting materials involved in the photocatalysts[1]. Photocatalytic activities are influenced by several properties of the semiconductor, such as the electronic bandgap, the dielectric constant, the charge carrier effective masses, and the exciton binding energy. In a general view, a good photocatalyst should meet three requirements simultaneously: a suitable electronic band gap to efficiently absorb visible sunlight which is between 2.1 and 2.8 eV depending on the targeted applications (water splitting, CO_2 reduction…),[2] a dielectric constant greater than 10 to obtain optimal value of exciton binding energy (E_b < 25 meV) and the carrier effective masses lower than 0.5 m_e in order to have a good mobility.[3] While band-gap engineering is a rather well-established approach, the charge carrier dynamics including their generation and diffusion is less commonly and systematically determined whereas it remains crucial for photocatalytic properties enhancement. In the present report, we propose to address this challenging aspect for two families of semi-conducting materials potentially interesting for photocatalytic applications.

Molybdenum disulfide (MoS_2) and molybdenum trioxide (MoO_3) as layered materials with strong intralayer iono-covalent bonding and weak van der Waals interlayer coupling, which gives the possibility to tune the number of stacked layers, garnered much research attention recently due to their rich physical and chemical properties beneficial for a wide range of applications[4] and attractive for new domains of energies.[5] Amongst the four various polymorphic phases of molybdenum trioxide [orthorhombic (α-MoO_3), monoclinic (β-MoO_3), hexagonal (h-MoO_3), and high pressure monoclinic (MoO_3-II)] [6], α-MoO_3 with the orthorhombic layered crystal structure and Pnma space group is thermodynamically most stable. α-MoO_3 is an n-type semiconductor with a wide experimental band gap of ~3.2 eV [7,8]. Due to its large band gap, α-MoO_3 has applications in numerous optical and electronic devices, including a transparent contact for organic photovoltaics or organic light-emitting diodes, photo- and electrochromic sensors, catalyst or gas sensor material and electrode material in

lithium batteries [9, 10, 11, 12, 13, 14, 15]. Nevertheless, α-MoO_3 can be activated under ultraviolet (UV) irradiation (λ<387 nm) only, which represents about 5% of solar energy and is not optimal to be used as photocatalyst for solar-energy applications directly. On the other hand, molybdenum disulfide (MoS_2) is a prototypical 2D layered transition metal dichalcogenide material that been studied extensively over recent decades for its photoelectrochemical [16], catalyst [17,18], energy storage [19] and photovoltaic [20] properties. The thermodynamically stable phase of MoS_2 among its three phases (1T, 2H, and 3R [21, 22]) is 2H phase with hexagonal crystal system and $P6_3/mmc$ space group. In its bulk form, 2H-MoS_2 is a semiconductor with an indirect band gap of about 1.23 eV [23] and therefore it is not a good candidate for photocatalysts. But, the combination of MoS_2 and MoO_3 materials can be found in photoelectrocatalysis [24]. The first reason of such combination is to build double-junction photocatalysts in which the combination of a large and low bandgap materials can lead to an efficient water splitting catalyst. The other reason explaining the existence of such junction is the synthesis of MoS_2 that can be done from MoO_3 leading to a core MoO_3 surrounded by MoS_2 [25]. The diffusion of O atoms from MoO_3 to MoS_2 and, reversely, the diffusion of S atoms from MoS_2 to MoO_3 can happen during the lifetime of such a device involving a MoS_2/MoO_3 junction. Understanding the effect of this phenomenon on the bulk properties of MoS_2 and MoO_3 materials seems an important topic of research to understand the long-term stability of a device involving this junction. The second reason is that in the course of the synthesis of MoS_2 phase from MoO_3 precursors, the formation of Mo-oxysulfide may take place which allows to tune the chemical composition of the materials [26]. This investigation can thus lead, as we will show later in text, to a proposition of new semiconductor composition.

Experimentally, Qin *et al*. showed that sulfur doping of molybdenum trioxide can improve the hole-transport properties of the host material [27]. Low concentration sulfur and selenium doping into α-MoO_3 was theoretically found to be an efficient way to yield band gap reduction and the enhanced optical absorptions in the visible and infrared regions [28]. However, it was shown that the low concentration level of S and Se-doping into α-MoO_3 could induce localized occupied states above the valence band in the electronic band structure and restrict the free carrier mobility in these systems which are unfavorable to enhance the photocatalytic efficiency. Hence, it is important to investigate if it is

possible to tune the effect of dopant concentration on the localized/delocalized character of the dopant levels as a function of the dopant concentration in order to optimize the electronic properties of the material.

On the other hand, the effects of oxygen doping MoS_2 nanosheets have received recent interest because of its applications as electrocatalysts for hydrogen evolution reaction (HER). It appears that oxygen doping of MoS_2 nanosheets reduces the energy barrier for H_2 evolution and increases the electric conductivity [29, 30, 31]. Previous work has shown that creating molybdenum trioxide defects by oxygen plasma treatment in the MoS_2 single-layer allows to tune the bandgap and control the optical properties [32]. Moreover, the band-gap of MoS_2 which is about 1.23 eV remains too small to make this material valuable for photocatalytic applications. It thus appears relevant to explore if O doped MoS_2 could help to improve the understanding of the increase of efficiency induced by such doping.

Herein, we aim to address the opto-electronic properties of O-doped 2H-MoS_2 and S-doped α-MoO_3 bulk systems in order to assess in one side the future potential of harnessing novel materials as a more efficient visible-light-driven photocatalysts and understand the effect of O doping in MoS_2 or S doping in MoO_3 on the other side. As aforementioned, we will particularly pay attention to the charge transport properties which are the most challenging aspects not so often addressed in the literature. The paper is organized as follows: in next section, the details of the computational methods employed to compute the crystal structure, electronic, charge transport and frequency depended optical properties are presented. Section 3 reports the results and discussion related to the structural properties of pristine and doped systems, the electronic and charge transport properties and the dielectric function and frequency dependent optical properties.

2. Computational Details

2.1 Total energy calculations

Total energy calculations including geometry optimizations of all structures were performed by periodic DFT using the PBE functional [33] and the Van der Waals contributions were described using the semi-empirical Grimme D3 approach [34] with optimized scaling factors (see supporting

information) as implemented in the *ab initio* CRYSTAL17 code. [35] Localized Gaussian-type function basis sets (BSs) were used: Mo_SC_HAYWSC-311(d31)G_cora_1997 [36] (for Mo atoms), S_86-311G*_lichanot_1993 [37] (for S atoms) and O_8-411d11G_valenzano_2006 [34] (for O atoms). All the electronic properties were computed using single-point calculations by using the range separated hybrid Heyd-Scuseria-Ernzehof (HSE06) [39] exchange correlation functional on the PBE optimized geometries. Calculations of the electronic and ionic contribution to the dielectric constant were performed by using the PBE functional as implemented in CRYSTAL17. Infinite Coulomb and exchange sums are truncated according to following five thresholds 8 8 8 8 16 [35]. The convergence criterion for the SCF cycle was fixed at 10^{-10} eV per unit-cell. Reciprocal space for unit-cell of MoS_2 and MoO_3 containing 6 and 16 atoms, respectively, is sampled according to a sublattice with a 12×12×8 and 8×12×12 *k*-point mesh for geometry optimization, electronic band structure and Coupled Perturbed Kohn-Sham (CPKS) [40] calculations. The *k*-point mesh sampling is progressively reduced as the size of the semiconductor unit cells increases for doped materials (see Table S1 and Table S2).

To identify the most stable $MoO_{3-x}S_x$ and $MoS_{2-x}O_x$ compositions as a function of the number of S- or O-atoms exchanged in the MoO_3 and MoS_2 structures respectively, we calculate the Grand potential, Ω, assuming that the reservoir surrounding the solids is constituted from ideal gas phase mixtures of H_2S/H_2O (commonly used experimentally as sulfiding and oxidizing agents) :

$MoO_3 + xH_2S = MoO_{(3-x)}S_x + xH_2O$ (1)

$MoS_2 + xH_2O = MoS_{(2-x)}O_x + xH_2S$ (2)

$$\Omega_{MoO_{3-x}S_x} = E_f(MoO_{3-x}S_x) - E_f(MoO_3) + xG^0_{f,T_0}(H_2O) - xG^0_{f,T_0}(H_2S) - xRT_0\ln\left[\frac{p(H_2S)}{p(H_2O)}\right] \quad (3)$$

$$\Omega_{MoS_{2-x}O_x} = E_f(MoS_{2-x}O_x) - E_f(MoS_2) + xG^0_{f,T_0}(H_2S) - xG^0_{f,T_0}(H_2O) - xRT_0\ln\left[\frac{p(H_2O)}{p(H_2S)}\right] \quad (4)$$

where E_f stands for the 0 K, formation energies of the different solids involved (neglecting vibrational and entropic contributions, see also supporting information), G^0_{f,T_0} stands for the Gibbs free energies of formation of H_2S and H_2O molecules (including thermal and entropic effects evaluated from NIST data base at T_0=298 K). So, for each value of x, we will plot the evolution of Ω_x as a function of the variable $\pm RT_0\ln\left[\frac{p(H_2O)}{p(H_2S)}\right]$ fixing the partial pressures of H_2S/H_2O in the reservoir assumed at T_0=298

K. Note that increasing T slightly diminishes the free enthalpy of oxidation reaction of MoS_2 while slightly increases the free enthalpy of sulfidation of MoO_3 (see supplementary information). However, the main trends reported at ambient T are only very weakly affected.

2.2 Transport properties

To quantify the carriers mobility, we computed the effectives masses (m_e^* and m_h^*) from two approaches: by fitting the bands with a parabolic function and by integrating the DOS. In the first model the electron and hole effective masses in various crystallographic directions can be calculated according to its band structure curvature at the extrema points [3] according to this formula:

$$E_{CB/VB}(\vec{k}) = E_{min} \pm \frac{\hbar^2}{2m_x^*}(k_x - k_{x-min})^2 \pm \frac{\hbar^2}{2m_y^*}(k_y - k_{y-min})^2 \pm \frac{\hbar^2}{2m_z^*}(k_z - k_{z-min})^2 \quad (5)$$

where $E_{CB/VB}$ is the conduction and valance bands eigenvalues, E_{min} is the energy at the extrema point, k are the k-space reciprocal lattice points, m_x^*, m_y^* and m_z^* are the effective masses along x, y and z directions, and $k_{i\text{-}min}$ is the band edge position in reciprocal space. The parabolic model has two main limitations: (i) the vicinity in energy of other band extrema and (ii) the adversity of an appropriate choice of crystallographic directions, therefore it cannot properly delineate effective masses [2]. The DOS-averaged effective mass using the semi-classical Boltzmann theory is the second approach adopted in this work which go beyond these limitations. The evaluation of the electronic transport properties was performed departing from the PBE-optimized geometry via single-point HSE06 calculations within the Boltzmann transport equation (BTE) involving a constant scattering time (τ = 10 fs) as implemented within CRYSTAL17 [41, 42]. For these properties we used a k-point mesh sampling at least 2 times denser than what we employed for geometry optimization in each structure.

2.3 Optical properties

The optical properties were calculated through the frequency-dependent dielectric matrix $\varepsilon_{\alpha\beta}(\omega)$, by using the Vienna ab initio Simulation Package (VASP)[43,44] and the methodology described in Ref. [45] and successfully applied to N- and S-doped TiO_2 materials [46,46,47]. For that purpose, we used the (HSE06) [39] exchange correlation functional a kinetic energy cut-off of 500 eV for the plane wave basis set and the project augmented wave (PAW)[10] pseudopotentials for Mo, O and S atoms. The optimized

structures obtained previously with CRYSTAL were used. The number of empty conduction bands (NBANDS) was converged for each structure with respect to standard calculations.

The absorption coefficient is calculated by using the following relationship:

$$\alpha_{\alpha\beta}(\omega) = \frac{2\omega k_{\alpha\beta}(\omega)}{c} = \frac{\omega \mathrm{Im}(\varepsilon_{\alpha\beta}(\omega))}{c n_{\alpha\beta}(\omega)} \qquad (6)$$

where c is the speed of light in vacuum. $n_{\alpha\beta}$ and $k_{\alpha\beta}$ are real and imaginary parts of the complex refractive index, and are known as the refractive index and the extinction index, respectively. They are given by the following relations:

$$n_{\alpha\beta}(\omega) = \sqrt{\frac{|\varepsilon_{\alpha\beta}(\omega)| + \mathrm{Re}(\varepsilon_{\alpha\beta}(\omega))}{2}} \qquad (7) \qquad k_{\alpha\beta}(\omega) = \sqrt{\frac{|\varepsilon_{\alpha\beta}(\omega)| - \mathrm{Re}(\varepsilon_{\alpha\beta}(\omega))}{2}} \qquad (8)$$

2.4 Exciton binding energy

The relative dielectric permittivity (ε_r) or more generally called relative dielectric constant results from the contribution of the electron density (ε_∞) and of the ion vibrations (ε_{vib}):

$$\varepsilon_r = \varepsilon_\infty + \varepsilon_{vib} \qquad (9)$$

The exciton binding energy (E_b) values for these structures are calculated in the framework of the Mott-Wannier model [48].

$$E_b = E_H \frac{m_r^*}{\varepsilon_r^2} \qquad (10)$$

where E_H is the energy of the 1s orbital of hydrogen (−13.6 eV) and m_r^* is the reduced mass of the exciton:

$$\frac{1}{m_r^*} = \frac{1}{m_e^*} + \frac{1}{m_h^*} \qquad (11)$$

3. Results

3.1 Energetic stability and structural properties

In the crystal structure of α-MoO_3 (Fig.1 (a)), where Mo atoms are an octahedral environment surrounded by 1 O-oxo species and 5 bridging O atoms. In 2H-MoS_2 (Fig.1 b), each Mo atom is in a trigonal prismatic environment surrounded by 6 S atoms shared themselves by 3 Mo atoms. To study the effects of sulfur doped α-MoO_3 and oxygen doped 2H-MoS_2 structures, different dopant concentrations were considered for both systems: S-substituted α-MoO_3 bulk with S concentration up

to 33% and O-substituted MoS_2 bulk with O concentration up to 75%. For high concentration of dopant, the stability of the native structure is suspected to be questioned. As detailed in supplementary information, we will consider that the complete MoO_3/MoS_2 inter-conversion can be prevented under controlled H_2S/H_2O environment. On the one hand, the oxidation of MoS_2 into MoO_3 is an endothermic process in H_2S/H_2O (this is not the case in O_2/SO_2 environment, as exemplified in supplementary information). On the other hand, the full sulfidation of MoO_3 into MoS_2 in H_2S/H_2O would require the presence of H_2. Furthermore, the 33% of S doping in MoO_3 corresponds to all oxo-terminal positions substituted by S (as discussed later in the text) keeping the internal cohesion of MoO_3 layers intact. Higher S-doping concentration would require substituting large concentration of bridging oxo, inducing the reconstruction of the native MoO_3 into more complex oxisulfides (amorphous) as suggested by experimental observations [49,50,51]. Such an investigation is beyond the scope of the present study.

For each doping level, several configurations were tested and only the properties of the most stable ones are presented in the text. Fig. 1 c and d illustrate two examples, for more information see the supporting information SI 2. Table S1 and S2 report the optimized lattice parameters and formation energies (E_f) of all studied S-substituted α-MoO_3 and O-substituted 2H-MoS_2 bulk systems, respectively. By increasing sulfur concentration, the MoO_3 lattice parameter (a) perpendicular to the basal plane of the layer increases while the in-plane lattice parameters (b and c) remain almost unchanged. In contrast, by increasing the O concentration in MoS_2, the c-parameter remains almost constant up to 50% O substitution. In order to discern on structural stability of these systems in more realistic conditions, we determine the thermodynamic phase diagrams (Fig. 2) of substituted systems with respect to the pristine structures by using the Grand potential approach. By using H_2O as oxygen source and H_2S as product (as used experimentally, see also Methods), the calculated reaction energies reveal that MoS_2 bulk oxidation is difficult particularly at high concentration (Figure S9). By contrast, the sulfidation of MoO_3 by H_2S is less difficult specially for S concentration higher than 17%. Fig. 2 (a) indicates that for a $RT_0 \ln\left[\frac{p(H_2S)}{p(H_2O)}\right]$ term greater than ~0.1 eV which corresponds to $\frac{p(H_2S)}{p(H_2O)}$ ~50, the pristine structure of MoO_3 becomes sulfided. For $RT_0 \ln\left[\frac{p(H_2S)}{p(H_2O)}\right]$ in the range 0.1-0.32 eV, the structure

with 25% S is the most stable. For $RT_0 \ln\left[\frac{p(H_2S)}{p(H_2O)}\right]$ higher than 0.32 eV, system with 33% S is thermodynamically favored. By contrast, Fig. 2 (b) shows that the oxidation of MoS_2 requires value of $RT_0 \ln\left[\frac{p(H_2O)}{p(H_2S)}\right]$ as high as 0.75 eV corresponding to $\frac{p(H_2O)}{p(H_2S)} \sim 10^{13}$, which implies that the MoS_2 pristine system should remain stable while the structure with the highest O concentration (the one tested here at 0.75%) should be favored. However, we cannot exclude that different oxidizing agents or reaction pathways may be used to make the oxidation process thermodynamically favorable. For instance, by using O_2 as oxidizer and SO_2 as a byproduct, it can be shown that reaction energies become exothermic and the thermodynamic diagram can be shifted to accessible reaction conditions (see Figure S10).

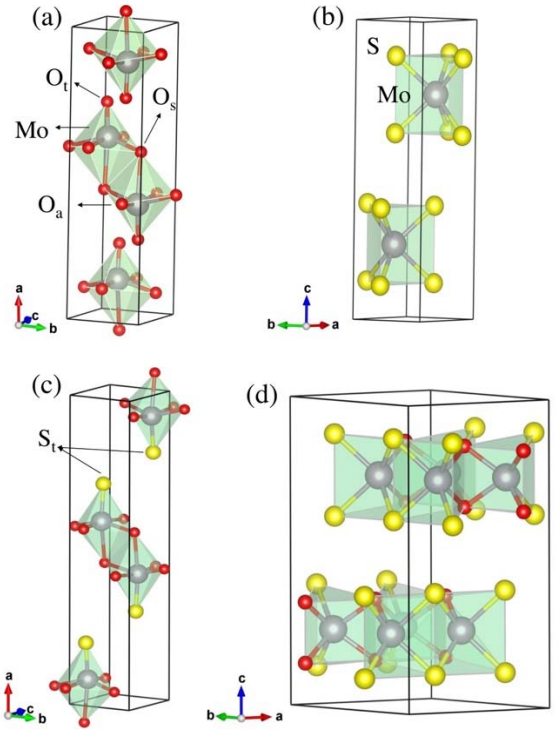

Fig. 1. The unit-cells of (a) α-MoO_3 (including 4 Mo and 12 O atoms), (b) 2H-MoS_2 (including 2 Mo and 4 S atoms) (c) α-MoO_2S (including 4 Mo, 8 O and 4 S) and (d) 2H-MoSO (including 8 Mo, 8 S and 8 O) structures. The three inequivalent oxygen atoms in α-MoO_3 structure are labeled: O_t is the apical oxygen atoms, O_a is the corner-sharing oxygen atoms and O_s is the edge-sharing oxygen atoms. While all S atoms in MoS_2 structure are equivalent. The purple, red and yellow balls in the geometrical models represent the Mo, O and S atoms, respectively.

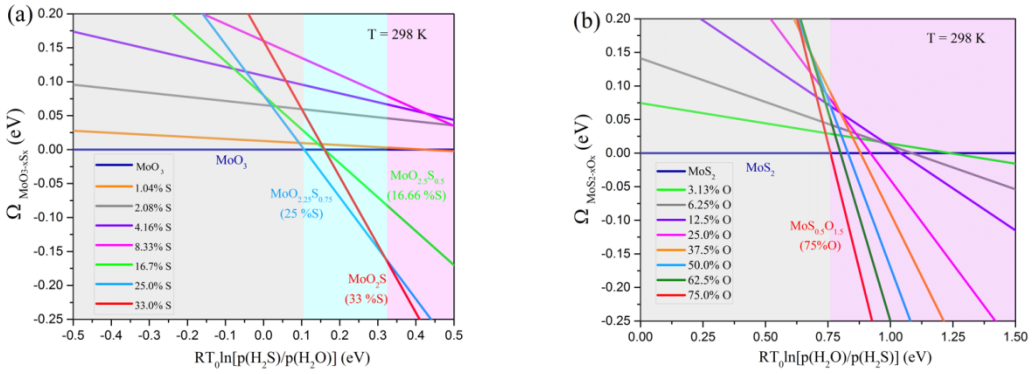

Fig. 2 Thermodynamic phase stability of the S-substituted α-MoO_3 (a) and O-substituted 2H-MoS_2 (b) bulk structures for different S- and O-concentrations with respect to pristine structures considering H_2S/H_2O reservoir

In term of bonding nature, the partial charge (Bader charge [52]) of S atoms in doped MoO_3 in absolute value is smaller than the one of oxygen atoms (~0.25 for S vs ~0.8 for O) highlighting the less ionic character of the Mo-S bond than the Mo-O bond, in agreement with the lower electronegativity of S versus O. The less ionic (and thus more covalent) character of the Mo-S bond than the Mo-O bond is also observed in O doped MoS_2 systems. This is further confirmed by the analysis of the redistribution of electron density in those systems (see Supporting Information Figure S11).

3.2 Electronic structure and absorption coefficient

To probe the electronic properties of S-doped α-MoO_3 and O-doped 2H-MoS_2, the band structures and the partial density of states (PDOS) of these systems have been calculated. Fig. 3 shows the band structure along the high symmetry directions and the projected density of states (PDOS) of pristine α-MoO_3 and 2H-MoS_2 structures and two relevant substituted systems for S-substituted α-MoO_3 with the concentration of 33% and O-substituted 2H-MoS_2 with the concentration of 50.0% obtained with HSE06. Both MoO_3 and MoS_2 exhibit an indirect bandgap with a computed value of 2.96 eV and 1.56 eV respectively, thus close to the reported experimental values of 3.0-3.2 eV [7,8] and 1.2-1.3 eV [53,54] respectively. A better agreement between theory and experiment could be possible by using a global hybrid functional involving a tuned exact exchange fraction (i.e. exact exchange equal to $1/\varepsilon_\infty$) with the positive point to give faster calculation than with the range separated hybrid functional HSE06 but with the main drawback to change the functional for any material [55,56,1]. In our work, we decided to

keep the same functional, HSE06, for all calculation even if a slight discrepancy between theory and experiment exists. The PDOS of α-MoO_3 bulk shows the top of the valence band (VB) is dominated by O 2p orbitals (Fig. 3 a), whereas the bottom of the conduction band (CB) is formed from Mo 4d orbitals with weak hybridization of O 2p states allowing us to conclude on the charge-transfer insulator character of this material. On the opposite, the PDOS of 2H-MoS_2 bulk indicates that both the top of the valence band and the bottom of the conduction band are dominated by Mo 4d orbitals with weak hybridization of S 3p states resulting in Mott insulator. This PDOS feature is induced by the trigonal prismatic environment of Mo atoms leading to the splitting of their 4d states into a_{1g} orbital located at the top of VB and e_g states at the bottom of CB. [57]

Upon substitution of O atoms by S atoms in α-MoO_3, a significant decrease of the energy gap is computed with values ranging from 1.61 eV to 1.87 eV depending on sulfur concentration (Fig. 4 (a) and Table S3) while keeping the indirect nature of the band gap. The abrupt band gap decreases induced even by the minimum sulfur doping considered originates from the appearance of sulfur state inside the MoO_3 pristine bandgap. In the Figure S12 in SI illustrates band structure and PDOS of the most stable S-substituted α-MoO_3 bulk structures. We found that at low sulfur concentration, the impurity bands are localized and situated above the VB maximum (in the band gap) of α-MoO_3. These impurity states originate from the 3p orbitals of S atom and restrict the free charge carrier mobility as it will be further discussed for concentration lower than 8.3%. For higher S-concentrations, such as 33% S (Fig. 3 c), the 3p orbitals of S atom are located at the top of the VB and starts to mix with the Mo 4d orbitals which may have positive effects on the mobility.

For O-doped MoS_2, it is found that substituting sulfur atoms with oxygen atoms for all concentrations does not produce significant change in band gap (Fig. 4 (b) and Table S4). Figure S16 illustrates band structures and PDOS and Table S4 summarized the optoelectronic properties of the most stable O-substituted 2H-MoS_2 bulk structures.

The fluctuation observed in the bandgap for large doping concentration for both MoS_2 and MoO_3 based materials probably originates from the choice to present only the most stable solid solution for each concentration. But even if there are some fluctuations in the bandgap, these variations remain in

the standard deviation of HSE06 (around 12%) [58,3] allowing us to conclude that the doping, at the concentrations considered, as a weak effect on MoO_3 and MoS_2 in term of bandgap.

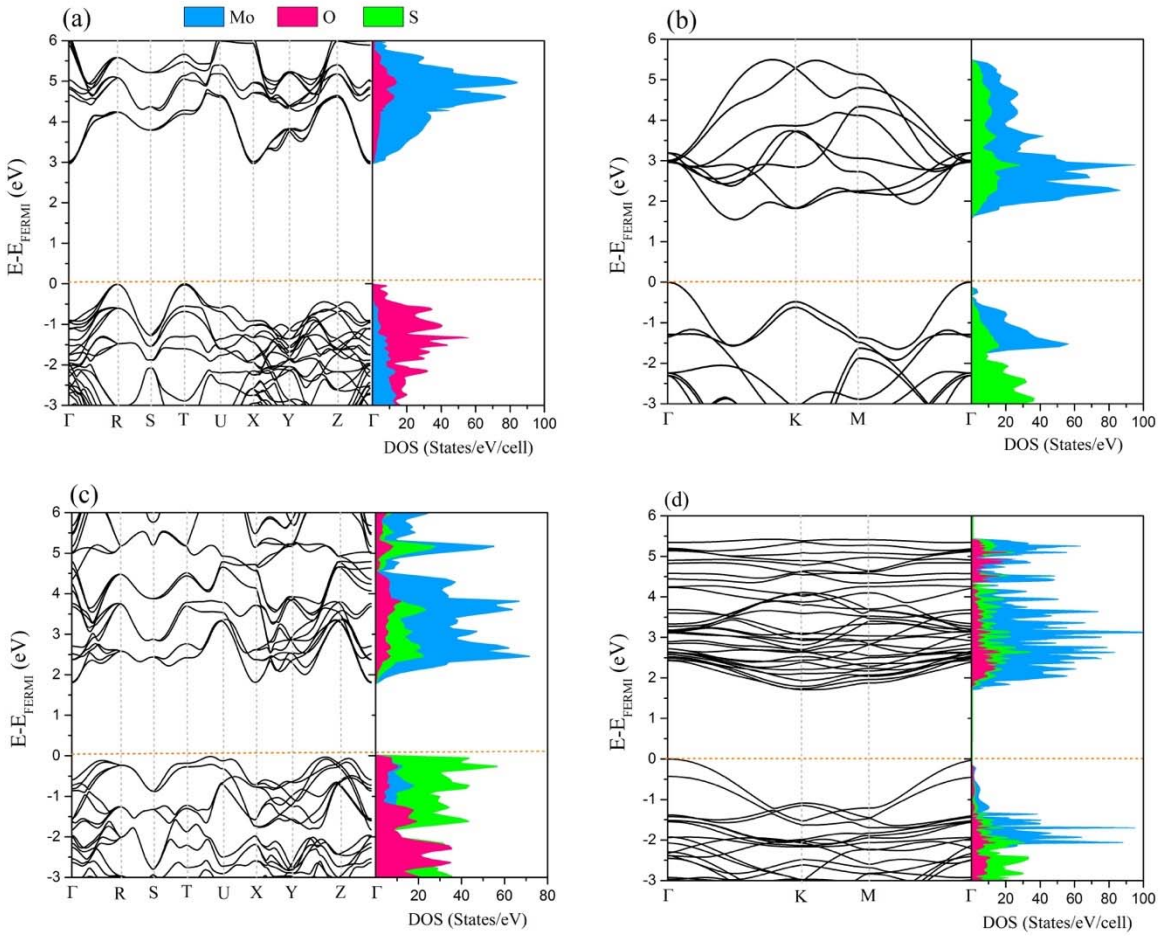

Fig. 3. Band structures and PDOS of α-MoO_3 (a), 2H-MoS_2 (b), α-MoO_2S (33%) (c) and 2H-MoSO (50%) (d) at HSE06 level. The Fermi level is set to zero.

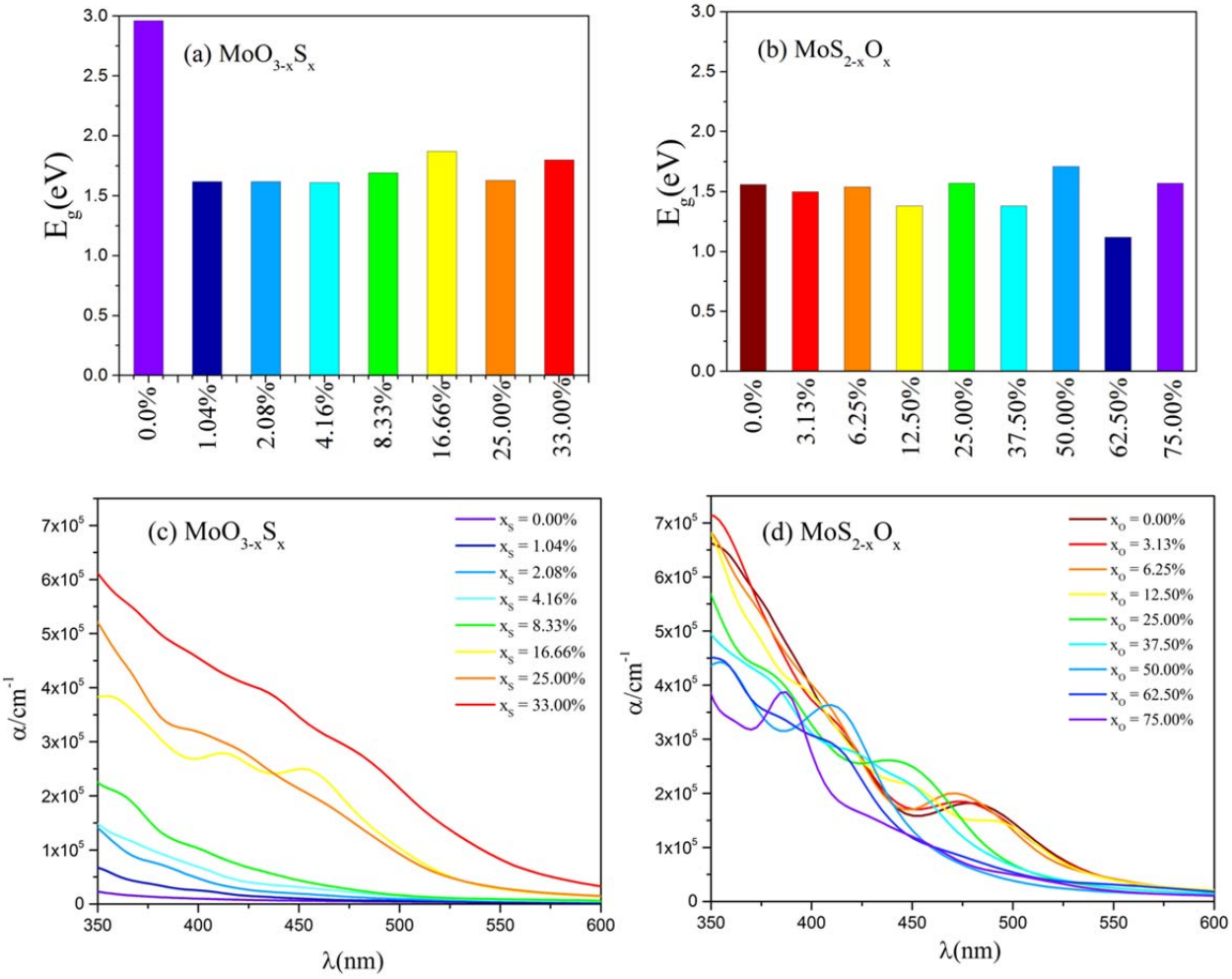

Fig. 4. Computed electronic band gaps (in eV) and absorption coefficient (α, in cm^{-1}) of the most stable S-substituted α-MoO_3 (a and c) and O-substituted 2H-MoS_2 (b and d) bulk structures for different S- and O-concentrations within HSE06.

The calculated absorption coefficients for pristine and doped systems (Fig. 4 and Fig. S18) show both highly anisotropic optical properties in these systems but with distinct anisotropic behaviors: the in-plane (within the layer) absorption coefficient in MoS_2 is larger than the absorption coefficient out of plane (in the interlayer direction) whereas the out-of-plane (perpendicular) is predominant in MoO_3 based materials (Fig. S18). However, the electronic band gaps for both substituted systems were found to be in the same range but the absorption spectra dramatically change by increasing the concentration of doping impurities. These results show that by enhancing S concentration the absorption coefficient of MoO_3 system is increased in the UV−vis window while it is reduced by increasing the O fraction on

MoS_2 system. For S-doped MoO_3, a strong increase of absorption coefficient is observed for S-concentration greater or equal to 16.7%, which makes this system interesting with that respect.

In general, despite the indirect band gap nature of S-doped MoO_3 and O-doped MoS_2 systems, the high absorption coefficients were attained (~10^5 cm^{-1}) for all structures except pristine α-MoO_3: this is higher than the typical absorption coefficient value for direct band gap semiconductors across the entire UV−vis range [59].

3.3 Charge transport

The charge carrier effective mass for α-MoO_3 along [100] (i.e. interlayer) direction are very large due to the dominance of Van der Waals (vdW) interactions between the layers in α-MoO_3 systems. The mobility of charge carriers in this interlayer direction is probably more governed by a polaronic model than a rigid band model assumed in the effective mass analysis. Thus, in the parabolic model for MoO_3, we only considered an average value which do not include [100] direction to calculate carriers effective mass. Table S3 listed the harmonic average of electron and hole effective masses for S-substituted α-MoO_3 systems along [010], [001] and [011] directions. The electron and hole effective masses for pristine α-MoO_3 bulk within the parabolic model are respectively 0.63 and 0.40 m_e, in a good agreement with previous theoretical data [60]. The electron effective mass obtained this method is slightly increased by increasing sulfur concentration while the hole effective mass is decreased. Table S3 also compares the effective mass of electron and hole obtained from DOS-averaged approach for S-substituted α-MoO_3 bulk system and the Boltzmann transport results are presented in Fig. S19. The electron and hole effective masses for pristine α-MoO_3 bulk within the DOS-averaged model are respectively 0.61 and 1.13 m_e leading to the mobility of 29 and 16 $cm^2V^{-1}s^{-1}$ for electrons and holes, respectively. As it can be seen from Fig. 5 and Table S3 the DOS-averaged electron effective masses for x_S = 1.04%, 2.08% and 4.16% are 3.78, 2.80 and 2.31 m_e resulting in mobilities of 5, 6 and 8 $cm^2V^{-1}s^{-1}$, respectively, which are significantly smaller than the electron mobility for pristine α-MoO_3. The corresponding hole effective mass values for the same concentrations are 4.75, 5.6 and 1.74 leading the hole mobility of 4, 3 and 10 $cm^2V^{-1}s^{-1}$. For higher concentration levels ($x_S \geq 16.7\%$), as previously discussed (Fig. 3 and S12), the 3p orbitals of S atoms are largely mixed with the 2p orbitals

of O atoms and 4d of Mo atoms nearby which eliminates localized impurity bands and increases carrier mobility. It is unveiled that due to the light DOS-averaged electron effective masses for x_s > 16.7%, the average electron mobility of these compounds is predicted to be reasonably high (especially for x_S=16.7% and x_S=33%). In general, for high sulfur concentrations, electrons were found to be more mobile than holes in S-doped α-MoO_3 systems. Moreover, for $x_S \geq 16.7\%$ the order of magnitude of charge carrier mobilities agrees well with the good charge collection efficiency.

Our results indicate that the carriers effective mass for MoS_2 compounds along the vdW interlayer direction are in the order of those along in-plane directions, hence all in-plane and out-of-plane directions have been taken into account to calculate carriers effective masses in parabolic model. The electron and hole effective masses obtained from parabolic model are 0.82 m_0 and 0.67 m_0 (Table S4), in a good agreement with previous work (m_e^* = 0.821 m_0 and m_h^* = 0.625 m_0) [61]. The corresponding values for m_e^* and m_h^* within DOS-averaged model are 0.38 m_0 and 0.23 m_0. The light electron and hole effective masses of pristine 2H-MoS_2 bulk lead to a desirable high electron and hole mobility (μ_e = 46 $cm^2\ V^{-1}s^{-1}$ and μ_h = 75 $cm^2\ V^{-1}s^{-1}$). From Fig. 5 and Table S4 it can be seen that by increasing substituting sulfur atoms with oxygen, the electron and hole effective masses are increased resulting in carriers mobility reduction. Nevertheless, the orders of magnitude of electron and hole mobilities for both pristine and O-doped systems agree well with a good charge collection efficiency. Among all these systems, MoSO structure (x_O = 50.0%) with wide band gap of 1.71 eV and high carrier mobility is the best option among all $MoS_{2-x}O_x$ systems for photocatalytic application.

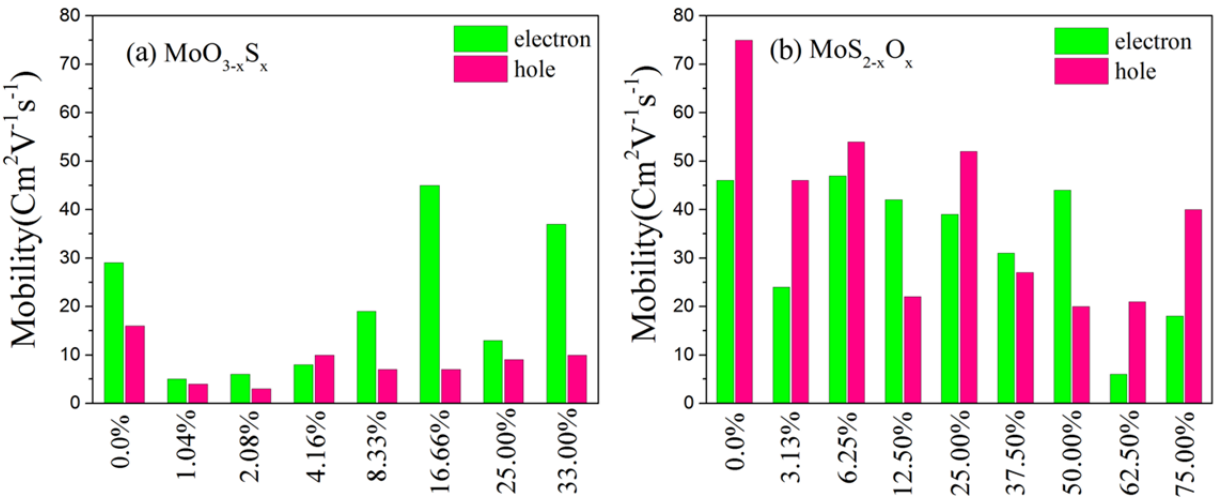

Fig. 5 Electron and hole mobility (in $Cm^2V^{-1}s^{-1}$) of the most stable S-substituted α-MoO_3 (a) and O-substituted 2H-MoS_2 (b) bulk structures for different S- and O-concentrations within HSE06.

3.4 Dielectric constant

As presented in the Introduction, a high relative dielectric constant (ε_r) correlates with a low binding energy (E_b) is necessary to dissociate the excitons into free charge carriers in semiconductors [3]. Tables S5 and S6 and Fig. 6 summarizes the calculated the electronic and relative dielectric constant (ε_∞ and ε_r) and exciton binding energy (E_b) of the most stable S-substituted α-MoO_3 bulk and O-substituted 2H-MoS_2 bulk structures. Both electronic contribution (ε_∞) and ionic vibrational contribution (ε_{vib}) for pristine bulk structures along the interlayer direction are smaller than those along in-plane directions. The geometric average of ε_∞ for pristine α-MoO_3 (5.6) is lower than 2H-MoS_2 (11.0) because of two correlated effects: sulfur is more polarizable than O and the Mo-S bond is more covalent than the Mo-O bond, as discussed before. In contrast, the large ε_{vib} computed in α-MoO_3 compared to MoS_2 bulk, comes from the larger ionic character of oxides than sulfides [32]. Furthermore, by increasing S concentration in both systems, ε_∞ increases mainly because sulfur atoms are more polarizable than oxygen atoms as said previously [62, 63]. By increasing sulfur concentration in α-MoO_3 structure, ε_r is enhanced from 13.9 for x_S =0.0% to 17.9 for x_S =33.0% thus within the range that is required for solar energy conversion ($\varepsilon_r > 10$) [3]. For 2H-MoS_2 structure the ε_r is decreased by increasing the oxygen

concentration from 11.1 for pristine structure to 8.9 for x_O = 75% that is reasonably high to consider these materials for photocatalytic application[3].

The exciton binding energy for pristine α-MoO_3 bulk (28 meV) increases for low sulfur doping concentrations ($x_S \leq 8.3\%$) due to the high value of m_r^* itself induced by the localized electronic states of the dopant. For high sulfur concentration levels ($x_S \geq 17\%$) the E_b significantly decreases because of high relative dielectric constant and low values for reduced effective masses. Especially for x_S = 17% and 33% the E_b is slightly lower than the determined threshold needed for charge carrier separation by thermal energy (25 meV at room temperature) together with low effective masses and large dielectric constant resulting in enhancement of the excitons dissociation efficiency.

The exciton binding energy of pristine 2H-MoS_2 is 16 meV, and in a good agreement with previous results (~20 meV) [64]. By increasing the O-doped concentration level into 2H-MoS_2 bulk the E_b is slightly increased for concentrations lower than 25% while it experiences a sharp increase for higher concentrations ($x_O \geq 37.5\%$). These results confirm that the oxygen content of MoS_2 must be kept as low as possible to maintain its good optoelectronic properties.

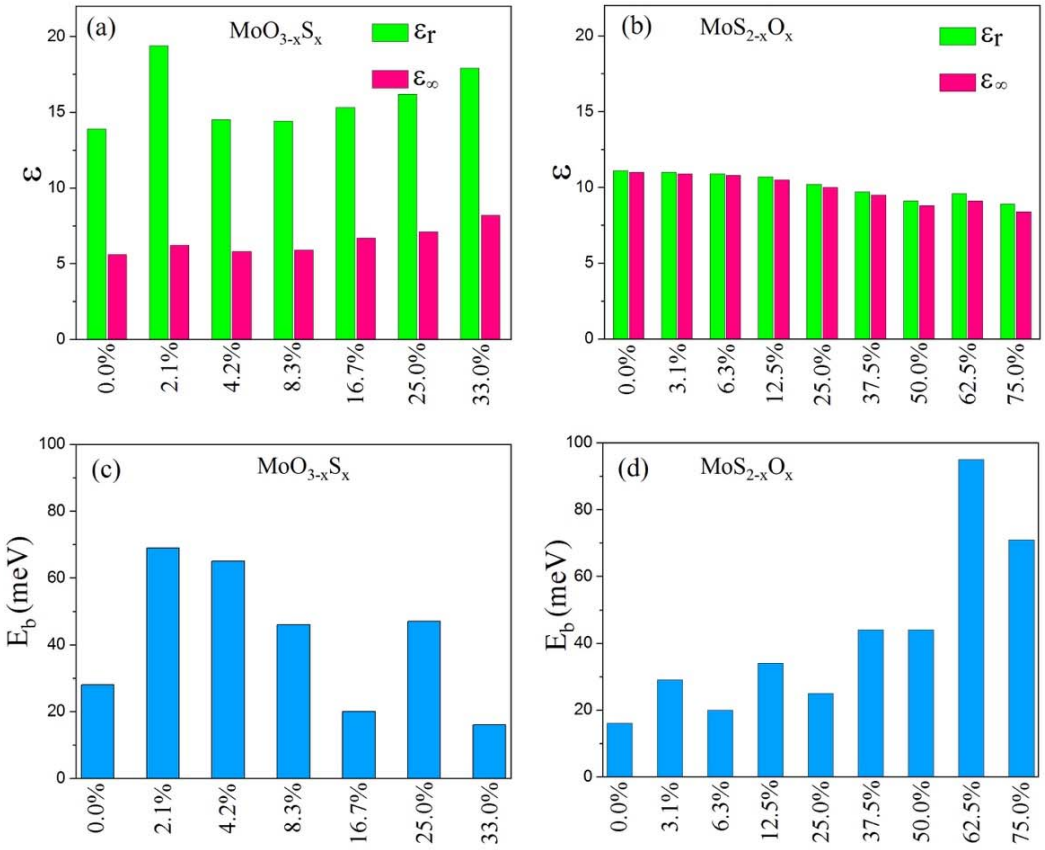

Fig. 6. Computed electronic dielectric constant (ε_∞), relative dielectric constant (ε_r) and exciton binding energy (in meV) of the most stable S-substituted α-MoO_3 and O-substituted 2H-MoS_2 bulk structures for different concentrations.

4. Conclusions

In summary, we performed a detailed first-principles calculation to study the structural, electronic, charge transport and optical properties of sulfur doped α-MoO_3 and oxygen doped MoS_2 bulk systems. In order to compare the stability of the various $MoO_{3-x}S_x$ structures in H_2S/H_2O environment which may be relevant for water splitting or CO_2 reduction, the phase diagram analysis revealed that MoO_3 with 25% and 33% S-(such as MoO_2S) concentrations can be thermodynamically stabilized under reasonable $\frac{p(H_2S)}{p(H_2O)}$ ratio. However, it appears that it is far more difficult to oxidize MoS_2 into $MoS_{2-x}O_x$ by using H_2O/H_2S environment, whereas it can become thermodynamically accessible by using O_2/S_α as the reactant/product pair. In this case, O-concentration as high as 75% may be reached.

Regarding opto-electronic properties, Table 1 summarizes the key calculated parameters of pristine α-MoO_3 and 2H-MoS_2 bulk systems with two relevant substituted structures (MoO_2S and MoSO).

	MoO_3	MoO_2S	MoS_2	MoSO
E_g (eV)	2.96	1.80	1.56	1.71
m_e^{*a} (m_e)	0.63	0.68	0.82	0.40
m_h^{*a} (m_e)	0.40	0.11	0.67	0.59
$m_{e\ DOS}^{*b}$ (m_e)	0.61	0.48	0.38	0.40
$m_{h\ DOS}^{*b}$ (m_e)	1.13	1.77	0.23	0.86
μ_e^c ($cm^2V^{-1}s^{-1}$)	29	37	46	44
μ_h^c ($cm^2V^{-1}s^{-1}$)	16	10	75	20
ε_∞	5.6	8.20	11.0	8.8
ε_r	13.9	17.90	11.1	9.1
E_b (meV)	28	16	16	44

Table 1. DFT calculated band gap energy, effective mass of electron and hole, DOS- averaged effective masses, electron and hole mobility, electronic dielectric constant (ε_∞), relative dielectric constant (ε_r) and exciton binding energy (E_b) of α-MoO_3, MoO_2S, 2H-MoS_2 and MoSO systems. [a]Harmonic average of different directions (see Table S3 and S4 for more information). [b] DOS- averaged effective masses and mobility obtained from the Boltzmann transport theory as implemented in CRYSTAL17 code and calculated at a carrier density of 10^{17} cm^{-3}. [c] The mobility was estimated under the assumption of τ = 10 fs.

Both MoO_3 and MoS_2 were confirmed to be indirect bandgap semiconductors with a 2.96 eV and 1.56 eV gap, respectively, by using the HSE06 functional in agreement with experimental data. As reported in Table 1 for the MoSO case (50% O), substituting sulfur atoms by oxygen atoms on 2H-MoS_2 does not produce significant change in the electronic band gap which may remain too low (E_g = 1.5-1.7 eV) for many applications (CO_2 reduction or H_2O splitting). Nevertheless, the oxygen substituted 2H-MoS_2 bulk systems with O-concentration up to 50% possess interesting properties: $\varepsilon_r \sim 8$, $\alpha > 10^5$ cm^{-1} and E_b = 20-60 meV compatible with some visible-light photocatalytic applications [3]. By

contrast, substituting the O_t sites in α-MoO_3 by sulfur atoms may significantly impact the electronic energy gap which decreases from ~3.0 eV in pristine material to around 1.6 eV in sulfur doped material. To avoid localized impurity states, our study suggests to use α-MoO_3 with sulfur concentrations higher than 17% possess good optical properties (Table 1): electronic band gap (~ 1.80 eV), dielectric function ($\varepsilon_r > 17$), optical absorption ($\alpha > 10^5$ cm^{-1}). Regarding charge mobility (μ_e=37, μ_h=10) and exciton binding energy (E_b ~ 16 meV), they are compatible with various photocatalytic applications. In order to attempt to further optimize the two MoO_3 and MoS_2 layered materials, we propose in future works to address how the calculated optical properties can be tuned by decreasing the number of stacked MoO_3 or MoS_2 layers, assumed to be infinite in the present work devoted to ideal bulk materials.

Acknowledgements:

This work is part of the "RatiOnAl Design for CATalysis" (ROAD4CAT) industrial chair, project IDEXLYON funded by the French National Research Agency (ANR-16-IDEX-0005) and the Commissariat-General for Investment (CGI) within the framework of Investissements d'Avenir program ("Investment for the future"). The authors thank the SYSPROD project and AXELERA Pôle de Compétitivité for financial support (PSMN Data Center). This work was granted access to the HPC resources of CINES, IDRIS and TGCC under the allocation 2018-080609 made by GENCI.

Supporting Information:

The supporting information contains the optimization of D3 correction parameters for MoS_2 and MoO_3; the details of the thermodynamic analysis; the bond nature analysis; the details of the optoelectronic properties of O-doped MoS_2 and S-doped MoO_3.

References

1 T. Le Bahers and K. Takanabe, *J. Photochem. Photobiol. C Photochem. Rev.*, 2019, **40**, 212–233.
2 A. T. Garcia-Esparza, N. Tymińska, R. A. R. A. Orabi and T. Le Bahers, *J. Mater. Chem. C*, 2019, **7**, 1612–1621.
3 T. Le Bahers, M. Rérat and P. Sautet, *J. Phys. Chem. C*, 2014, **118**, 5997–6008.
4 All, Catalysis by Transition Metal Sulphides - RAYBAUD Pascal - TOULHOAT Hervé, http://www.editionstechnip.com/fr/catalogue-detail/1176/catalysis-by-transition-metal-sulphides.html, (accessed November 27, 2019).
5 C. G. Morales-Guio, L.-A. Stern and X. Hu, *Chem. Soc. Rev.*, 2014, **43**, 6555–6569.
6 A. S. Etman, H. N. Abdelhamid, Y. Yuan, L. Wang, X. Zou and J. Sun, *ACS Omega*, 2018, **3**, 2193–2201.
7 P. F. Carcia and E. M. McCarron, *Thin Solid Films*, 1987, **155**, 53–63.
8 M. Kröger, S. Hamwi, J. Meyer, T. Riedl, W. Kowalsky and A. Kahn, *Appl. Phys. Lett.*, 2009, **95**, 123301.
9 C.-W. Chu, S.-H. Li, C.-W. Chen, V. Shrotriya and Y. Yang, *Appl. Phys. Lett.*, 2005, **87**, 193508.
10 Q. Y. Bao, J. P. Yang, Y. Q. Li and J. X. Tang, *Appl. Phys. Lett.*, 2010, **97**, 063303.
11 J. N. Yao, K. Hashimoto and A. Fujishima, *Nature*, 1992, **355**, 624–626.
12 N. A. Chernova, M. Roppolo, A. C. Dillon and M. S. Whittingham, *J. Mater. Chem.*, 2009, **19**, 2526–2552.
13 R. Rousseau, D. A. Dixon, B. D. Kay and Z. Dohnálek, *Chem. Soc. Rev.*, 2014, **43**, 7664–7680.
14 S.-H. Lee, Y.-H. Kim, R. Deshpande, P. A. Parilla, E. Whitney, D. T. Gillaspie, K. M. Jones, A. H. Mahan, S. Zhang and A. C. Dillon, *Adv. Mater.*, 2008, **20**, 3627–3632.
15 H. Peelaers, M. L. Chabinyc and C. G. Van de Walle, *Chem. Mater.*, 2017, **29**, 2563–2567.
16 A. Ali, F. A. Mangrio, X. Chen, Y. Dai, K. Chen, X. Xu, R. Xia and L. Zhu, *Nanoscale*, 2019, **11**, 7813–7824.
17 B. Baubet, M. Girleanu, A.-S. Gay, A.-L. Taleb, M. Moreaud, F. Wahl, V. Delattre, E. Devers, A. Hugon, O. Ersen, P. Afanasiev and P. Raybaud, *ACS Catal.*, 2016, **6**, 1081–1092.
18 G. Li, D. Zhang, Q. Qiao, Y. Yu, D. Peterson, A. Zafar, R. Kumar, S. Curtarolo, F. Hunte, S. Shannon, Y. Zhu, W. Yang and L. Cao, *J. Am. Chem. Soc.*, 2016, **138**, 16632–16638.
19 A. H. Reshak and S. Auluck, *Phys. Rev. B*, 2003, **68**, 125101.
20 E. Fortin and W. M. Sears, *J. Phys. Chem. Solids*, 1982, **43**, 881–884.
21 X. Guo, G. Yang, J. Zhang and X. Xu, *AIP Adv.*, 2015, **5**, 097174.
22 M. Xu, T. Liang, M. Shi and H. Chen, *Chem. Rev.*, 2013, **113**, 3766–3798.
23 K. K. Kam and B. A. Parkinson, *J. Phys. Chem.*, 1982, **86**, 463–467.
24 H. Li, K. Yu, Z. Tang, H. Fu and Z. Zhu, *Phys. Chem. Chem. Phys.*, 2016, **18**, 14074–14085.
25 Z. Chen, D. Cummins, B. N. Reinecke, E. Clark, M. K. Sunkara and T. F. Jaramillo, *Nano Lett.*, 2011, **11**, 4168–4175.
26 A. D. Gandubert, E. Krebs, C. Legens, D. Costa, D. Guillaume and P. Raybaud, *Catal. Today*, 2008, **130**, 149–159.
27 P. Qin, G. Fang, F. Cheng, W. Ke, H. Lei, H. Wang and X. Zhao, *ACS Appl. Mater. Interfaces*, 2014, **6**, 2963–2973.
28 S. Bandaru, G. Saranya, N. J. English, C. Yam and M. Chen, *Sci. Rep.*, 2018, **8**, 10144.
29 H. Lin, Y. Li, H. Li and X. Wang, *Nano Res.*, 2017, **10**, 1377–1392.

30 J. Xie, J. Zhang, S. Li, F. Grote, X. Zhang, H. Zhang, R. Wang, Y. Lei, B. Pan and Y. Xie, *J. Am. Chem. Soc.*, 2013, **135**, 17881–17888.
31 W. Shi and Z. Wang, *J. Taiwan Inst. Chem. Eng.*, 2018, **82**, 163–168.
32 N. Kang, H. P. Paudel, M. N. Leuenberger, L. Tetard and S. I. Khondaker, *J. Phys. Chem. C*, 2014, **118**, 21258–21263.
33 J. P. Perdew, K. Burke and M. Ernzerhof, *Phys. Rev. Lett.*, 1996, **77**, 3865–3868.
34 A consistent and accurate ab initio parametrization of density functional dispersion correction (DFT-D) for the 94 elements H-Pu: The Journal of Chemical Physics: Vol 132, No 15, https://aip.scitation.org/doi/10.1063/1.3382344, (accessed July 11, 2019).
35 R. Dovesi, A. Erba, R. Orlando, C. M. Zicovich-Wilson, B. Civalleri, L. Maschio, M. Rérat, S. Casassa, J. Baima, S. Salustro and B. Kirtman, *Wiley Interdiscip. Rev. Comput. Mol. Sci.*, 2018, **8**, e1360.
36 F. Corà, A. Patel, N. M. Harrison, C. Roetti and C. R. A. Catlow, *J. Mater. Chem.*, 1997, **7**, 959–967.
37 Quantum Mechnical Hartree-Fock Study of the Elastic Properties of Li2S and Na2S | Scinapse | Academic search engine for paper, https://scinapse.io/papers/1972451189, (accessed July 11, 2019).
38 L. Valenzano, F. J. Torres, K. Doll, F. Pascale, C. M. Zicovich-Wilson and R. Dovesi, *Z. Für Phys. Chem.*, 2006, **220**, 893–912.
39 J. Heyd and G. E. Scuseria, *J. Chem. Phys.*, 2004, **121**, 1187–1192.
40 R. Orlando, V. Lacivita, R. Bast and K. Ruud, *J. Chem. Phys.*, 2010, **132**, 244106.
41 J. Linnera, G. Sansone, L. Maschio and A. J. Karttunen, *J. Phys. Chem. C*, 2018, **122**, 15180–15189.
42 G. Sansone, A. Ferretti and L. Maschio, *J. Chem. Phys.*, 2017, **147**, 114101.
43 G. Kresse and J. Furthmüller, *Phys. Rev. B*, 1996, **54**, 11169–11186.
44 G. Kresse and J. Furthmüller, *Comput. Mater. Sci.*, 1996, **6**, 15–50.
45 M. Gajdoš, K. Hummer, G. Kresse, J. Furthmüller and F. Bechstedt, *Phys. Rev. B*, 2006, **73**, 045112.
46 M. Harb, P. Sautet and P. Raybaud, *J. Phys. Chem. C*, 2013, **117**, 8892–8902.
47 M. Harb, P. Sautet and P. Raybaud, *J. Phys. Chem. C*, 2011, **115**, 19394–19404.
48 I. Pelant and J. Valenta, *Luminescence Spectroscopy of Semiconductors*, Oxford University Press, 2012.
49 T. Weber, J. C. Muijsers, J. H. M. C. van Wolput, C. P. J. Verhagen and J. W. Niemantsverdriet, *J. Phys. Chem.*, 1996, **100**, 14144–14150.
50 D. Genuit, I. Bezverkhyy and P. Afanasiev, *J. Solid State Chem.*, 2005, **178**, 2759–2765.
51 T. Weber, J. C. Muijsers and J. W. Niemantsverdriet, *J. Phys. Chem.*, 1995, **99**, 9194–9200.
52 G. Henkelman, A. Arnaldsson and H. Jónsson, *Comput. Mater. Sci.*, 2006, **36**, 354–360.
53 B. Radisavljevic, A. Radenovic, J. Brivio, V. Giacometti and A. Kis, *Nat. Nanotechnol.*, 2011, **6**, 147–150.
54 K. F. Mak, C. Lee, J. Hone, J. Shan and T. F. Heinz, *Phys. Rev. Lett.*, 2010, **105**, 136805.
55 J. C. Conesa, *Catal. Today*, 2013, **208**, 11–18.
56 J. H. Skone, M. Govoni and G. Galli, *Phys. Rev. B*, 2014, **89**, 195112.
57 P. Raybaud, J. Hafner, G. Kresse and H. Toulhoat, *J. Phys. Condens. Matter*, 1997, **9**, 11107–11140.
58 A. Stoliaroff and C. Latouche, *J. Phys. Chem. C*, 2020, **124**, 8467–8478.
59 P. YU and M. Cardona, *Fundamentals of Semiconductors: Physics and Materials Properties*, Springer-Verlag, Berlin Heidelberg, 4th edn., 2010.
60 B. S. Dandogbessi and O. Akin-Ojo, *J. Appl. Phys.*, 2016, **120**, 055105.
61 C. Habenicht, M. Knupfer and B. Büchner, *Phys. Rev. B*, 2015, **91**, 245203.

62 E. Schaumann, in *Sulfur-Mediated Rearrangements I*, ed. E. Schaumann, Springer Berlin Heidelberg, Berlin, Heidelberg, 2007, pp. 1–34.
63 F. Bernardi, I. G. Csizmadia, A. Mangini, H. B. Schlegel, M.-H. Whangbo and S. Wolfe, *J. Am. Chem. Soc.*, 1975, **97**, 2209–2218.
64 N. Saigal, V. Sugunakar and S. Ghosh, *Appl. Phys. Lett.*, 2016, **108**, 132105.

Table of Contents